Ultra-coarse-graining of homopolymers in inhomogeneous systems

Fabian Berressem[1] , **Christoph Scherer**[2] , **Denis Andrienko**[2] and
Arash Nikoubashman[1],*

[1] Institute of Physics, Johannes Gutenberg University Mainz, Staudingerweg 7, 55128 Mainz, Germany
[2] Max Planck Institute for Polymer Research, Ackermannweg 10, 55128 Mainz, Germany

E-mail: anikouba@uni-mainz.de

CrossMark

Abstract

We develop coarse-grained (CG) models for simulating homopolymers in inhomogeneous systems, focusing on polymer films and droplets. If the CG polymers interact solely through two-body potentials, then the films and droplets either dissolve or collapse into small aggregates, depending on whether the effective polymer–polymer interactions have been determined from reference simulations in the bulk or at infinite dilution. To address this shortcoming, we include higher order interactions either through an additional three-body potential or a local density-dependent potential (LDP). We parameterize the two- and three-body potentials via force matching, and the LDP through relative entropy minimization. While the CG models with three-body interactions fail at reproducing stable polymer films and droplets, CG simulations with an LDP are able to do so. Minor quantitative differences between the reference and the CG simulations, namely a slight broadening of interfaces accompanied by a smaller surface tension in the CG simulations, can be attributed to the deformation of polymers near the interfaces, which cannot be resolved in the CG representation, where the polymers are mapped to spherical beads.

Keywords: coarse-graining, polymer, thin films, droplets, local density dependent potential, three-body potential, inhomogeneous system

S Supplementary material for this article is available online

(Some figures may appear in colour only in the online journal)

1. Introduction

Coarse-graining is a systematic approach to reduce the number of degrees of freedom for building a simplified model of a system which reproduces its essential physical properties. The major advantage of coarse-grained (CG) models is that they provide access to longer simulation time- and length-scales, by reducing the number of interaction sites and introducing softer interaction potentials which accelerate the dynamics. Numerous CG models have been developed for simulating, e.g., polymer melts [1–3], organic solvents [4–6], lipid membranes

[7, 8], conjugated polymers [9–14], peptides [15], surfactants [16], and proteins [17].

CG potentials can be viewed as a projection of a many-body potential of mean force onto a CG force field [18, 19]. This projection is, however, not unique, as it depends on the thermodynamic or structural properties which should be preserved. Coarse-graining based on, e.g., reproducing entropy [20–23], forces [18, 19, 24, 25], or structure [26, 27] usually leads to distinct CG models of the system as the projection to a CG potential is in general not unique. In the limit of a complete set of CG basis functions, the different techniques will indeed lead to the same true many-body CG potential of mean force. However, this equivalency does not apply to practical cases of

---

* Author to whom any correspondence should be addressed.

relevance with a limited CG basis set, as structure- and relative entropy-based CG methods minimize a different functional than force matching (FM) methods [19, 21]. Further, although there is a one-to-one relation between the pair structure and two-body potentials [28], such associations generally do not hold for higher order structural correlations and potentials. As a result, different parametrization schemes can lead to different CG potentials [29], and therefore CG models cannot represent all features of the original reference systems (representability problem). Further, CG models are typically optimized at one specific state point, e.g., a certain temperature and/or pressure, and are therefore not necessarily suited for studying the same system at a different state point (transferability problem) [30, 31]. Finally, the CG force fields should be computationally efficient to compensate for the loss in molecular details.

While a fairly coherent understanding of bottom-up coarse-graining based on structural correlations or inter-atomic forces has been established for *homogeneous* liquids in the *bulk* [19], one is often interested in phenomena taking place at interfaces, which are much less understood. Typical examples are wetting films or droplets and aqueous/organic interfaces in biological cells [32, 33]. These systems are intrinsically inhomogeneous, either in density or other local descriptors. Apart from these examples, CG models are particularly sensitive to local density fluctuations, even in bulk systems, due to their softer interaction potentials and smaller number of particles [34–36]. Local inhomogeneity imposes extra demands on the CG model, in particular its tolerance to density variations [37–39]. Higher-order many-body expansions [40–45] and an explicit density dependence of interaction potentials [30, 39, 46–49] are two straightforward approaches that can improve transferability of CG models. These improvements have, however, different accuracy and computational overhead.

The aim of this work is to compare the accuracy and efficiency of two CG models for simulating homopolymers in inhomogeneous systems, such as thin films or droplets. These systems are characterized by large surface-to-volume ratios and strong density variations near the polymer–solvent interface. The first model incorporates three-body Stillinger–Weber basis functions, while the second has an explicit local density dependence. We show that the three-body expansion is computationally demanding and does not lead to stable interfaces. In contrast, the local density potential is capable of reproducing properties of inhomogeneous systems without a significant computational overhead.

The remainder of this manuscript is organized as follows: in section 2.1 we present our reference systems, while we have summarized the employed coarse-graining methods in section 2.2. The resulting two- and many-body interactions of the CG models are discussed in sections 3.1–3.3, and the properties of the CG simulations are analyzed and compared to the reference simulations in section 3.4. Section 4 provides a brief summary of our main findings and an outlook on planned extensions of our model.

2. Methods

2.1. Microscopically resolved reference systems

The microscopically resolved (MR) reference systems consisted of N_p homopolymers dispersed in an implicit solvent. Polymers were represented by a generic bead-spring model with $N = 20$ monomers per chain. Non-bonded interactions between the monomers were modeled using the Lennard-Jones (LJ) potential:

$$U^{\mathrm{LJ}}(r_{ij}) = \begin{cases} 4\varepsilon \left[\left(\dfrac{\sigma}{r_{ij}} \right)^{12} - \left(\dfrac{\sigma}{r_{ij}} \right)^{6} \right], & r_{ij} < r_{\mathrm{c}} \\ 0, & r_{ij} \geqslant r_{\mathrm{c}} \end{cases} \quad (1)$$

with radial distance r_{ij} between particles i and j, interaction strength $\varepsilon = k_{\mathrm{B}}T$, and bead diameter σ. The potential was truncated at the cutoff radius of $r_{\mathrm{c}} = 5\sigma$.

Polymer bonds were modeled through the finitely extensible nonlinear elastic (FENE) potential: [50]

$$U^{\mathrm{FENE}}(r_{ij}) = \begin{cases} -\dfrac{1}{2} k r_0^2 \ln \left[1 - \left(r_{ij}/r_0 \right)^2 \right], & r_{ij} < r_0 \\ \infty, & r_{ij} \geqslant r_0 \end{cases}$$
$$(2)$$

with spring constant $k = 30\, k_{\mathrm{B}}T/\sigma^2$ and maximum bond extension $r_0 = 1.5\sigma$ [51].

All MD simulations were conducted in the $\mathcal{N}VT$ ensemble (unless stated otherwise explicitly), $\mathcal{N} = N_{\mathrm{p}}N$ being the total number of monomers in the system. The temperature was kept constant at $T = 1.0\varepsilon/k_{\mathrm{B}}$ through a Langevin thermostat with friction coefficient $\xi = 1.0\, m/\tau$, where m is the monomer mass, and $\tau = \sqrt{m\sigma^2/(k_{\mathrm{B}}T)}$ is the unit of time. The equations of motion were integrated using a Verlet scheme with time step $\Delta t = 0.001\,\tau$. All simulations were conducted in cubic simulation boxes with edge length L and periodic boundary conditions in all three Cartesian directions.

To characterize the polymer properties in homogeneous systems, we simulated a bulk polymer melt with $N_{\mathrm{p}} = 2000$ chains. The melt was first equilibrated in the $\mathcal{N}PT$ ensemble at a pressure of $P = 0\, k_{\mathrm{B}}T/\sigma^3$, resulting in an average monomer number density of $\rho_{\mathrm{b}} = 0.921\,\sigma^{-3}$ (all quantities extracted from bulk simulations will be denoted by a subscript 'b', while the subscript '0' marks quantities obtained or parameterized at infinite dilution). Once the system reached equilibrium, we switched to the $\mathcal{N}VT$ ensemble using a cubic simulation box with $L = 35.15\,\sigma$, and simulated for 2×10^7 time steps, saving configurations and taking measurements every 1000 time steps. We characterized the conformation of the polymers through the average radius of gyration tensor:

$$\mathbf{G} = \frac{1}{N} \sum_{i=1}^{N} \langle \Delta \mathbf{r}_i \otimes \Delta \mathbf{r}_i \rangle \quad (3)$$

where $\Delta \mathbf{r}_i$ is the vector from the polymer center of mass to monomer i, and $\otimes$ indicates the dyadic product. The radius of

Table 1. Number of homopolymers N_p in polymer films and droplets, with measured thickness H and radius R, respectively.

System	N_p	$L [\sigma]$	H or $R [\sigma]$
Film	365	28.8	9.6
Film	728	33.2	14.4
Film	1245	37.6	19.2
Droplet	143	31.6	8.5
Droplet	482	40.4	13.0
Droplet	1142	49.2	17.6
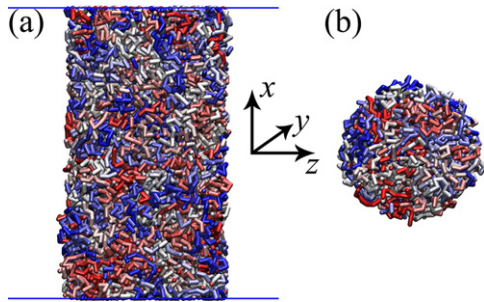
Figure 1. Simulation snapshots of (a) a thin film with thickness $H = 8 R_{g,b}$, and (b) a droplet with radius $R = 4 R_{g,b}$ from the MR reference simulations. The chains are colored differently for better distinction. Snapshots have been rendered using visual molecular dynamics v.1.9.3 [53].

gyration is then $R_g = \sqrt{G_{xx} + G_{yy} + G_{zz}}$, with $R_{g,b} \approx 2.2\,\sigma$ in the bulk simulations.

Thin films were constructed by initially placing the polymers in a slab at the center of the simulation box, so that the normal vectors of the polymer–solvent interfaces lied parallel to the z-axis. The polymer droplets were created similarly by initializing the polymers close to each other in the box center. The size of the simulation boxes was chosen sufficiently large to prevent nonphysical self-interactions and the coalescence of the films/droplets with their periodic images (see table 1). Simulations were then performed in the $\mathcal{N}VT$ ensemble at $T = 1.0\,\varepsilon/k_B$. This state point falls inside the two-phase coexistence region of the system [52], so that the polymers separated into a high and low density phase that coexisted in the same simulation box. Simulation snapshots of typical films and droplets from the MR simulations are shown in figure 1. We determined the film thicknesses H and droplet diameters $2R$ from the full width at half maximum of the monomer density profiles (see figure 2(a)). The resulting H and R values are summarized in table 1, and they are in good agreement with the estimates $H = \mathcal{N}/(L^2 \rho_b)$ and $R = [3\mathcal{N}/(4\pi\rho_b)]^{1/3}$, respectively, which assume a homogeneous monomer density inside the films/droplets and a perfectly sharp polymer–solvent interface.

Figure 2(a) shows the monomers number density along the film normal, $\rho(z)$, for the system containing $N_p = 1245$ homopolymers (the data for the thinner films look qualitatively similar and have been omitted for brevity). Since the simulated temperature was far below the critical temperature of this system ($T_c \approx 2.65\,\varepsilon/k_B$ [52]), all polymers were part of the thin

film (the density in the 'vapor' phase was strictly zero in our simulations). The density profile has a flat plateau with density $\rho = 0.922\,\sigma^{-3}$, which is in excellent agreement with the value measured in the bulk systems ($\rho_b = 0.921\,\sigma^{-3}$). Measurement uncertainties of the density profiles were estimated from the standard error of the mean between ten subdivided blocks of the data. Note that we did not determine the (apparent) width of the polymer–solvent interfaces, as this measurement would only be meaningful when the dependence on the lateral box dimensions is analyzed to account for the broadening due to capillary waves [54].

The density profile of the polymer centers of mass, $\rho_p(z)$, is also flat in the bulk-like interior of the film, but has two distinct peaks at $z = \pm 8\,\sigma$, indicating a surplus of polymers near the polymer–solvent interfaces (figure 2(a)). This local excess of polymers can be rationalized by considering the conformation of the individual chains, which we have characterized via the diagonal components of the radius of gyration tensor (figure 2(b)). The polymers are essentially isotropic in the central region of the film, but they assume an oblate ellipsoidal shape near the edges of the film, with $G_{zz} < G_{yy} = G_{xx}$ and a maximum aspect ratio of about $G_{xx}/G_{zz} \approx 4$.

Finally, we determined the surface tension of the thin films from the anisotropy of the pressure tensor:

$$\gamma = \frac{L_z}{2} \left\langle P_{zz} - \frac{P_{xx} + P_{yy}}{2} \right\rangle \qquad (4)$$

where $P_{\alpha\alpha}$ denotes the diagonal components of the instantaneous pressure tensor, which was computed from the Clausius virial equation. The factor of $1/2$ in equation (4) is due to the presence of two interfaces (see figure 1(a)). Here, we find a value of $\gamma = 1.42\,k_B T/\sigma^2$ for all three investigated film thicknesses.

### 2.2. Coarse-graining procedure

In our CG model, an entire homopolymer chain is represented by a single spherical particle, as depicted in figure 3. We tested three different approaches, using (i) only two-body interactions, (ii) a combination of two-body and three-body interactions, and (iii) a combination of two-body and (mean-field) many-body interactions. In the following, we briefly discuss these interactions and how they have been parameterized. The resulting CG potentials are then presented in section 3.

2.2.1. Two-body interaction. In all models, the pairwise interactions were determined using FM [18, 24, 25], where the force on each CG bead is calculated as the sum of the forces on the monomers of the corresponding polymer. We determined the two-body interaction potentials between the CG polymers using FM from bulk simulations, U_b^{2b}, as well as from simulations containing two isolated polymers, U_0^{2b}. The first approach results in a pair potential that (implicitly) includes many-body effects due to the surrounding polymers, while the second approach provides the pairwise interaction of only two polymer chains.

We introduced a cutoff radius, r_c^{2b}, beyond which the CG particles do not interact with each other. The two-body
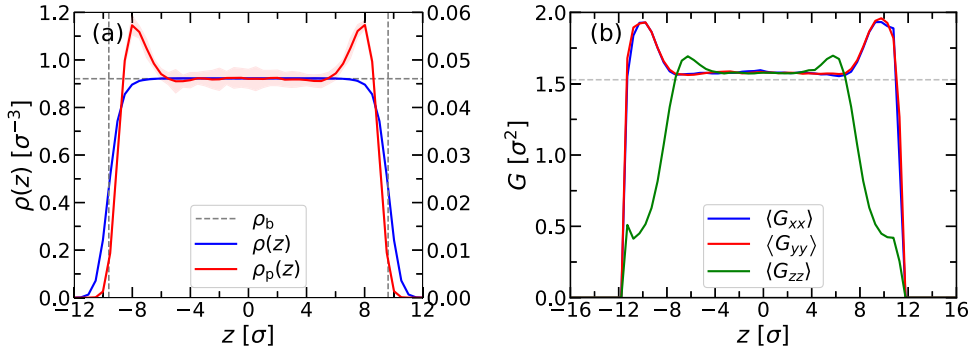
Figure 2. (a) Number density profiles of monomers (ρ, left axis) and polymer centers of mass (ρ_p, right axis) as functions of z. The horizontal dashed line indicates the monomer number density in the bulk system. The vertical dashed lines indicate the positions where $\rho(z)$ drops to half of its maximum value. (b) Diagonal components of the radius of gyration tensor, $G_{\alpha\alpha}$, as functions of z. The horizontal dashed line indicates the value of $G_{\alpha\alpha}$ in the bulk simulation. Data shown for a film with thickness $H \approx 8\,R_{g,b}$, consisting of $N_p = 1245$ homopolymers.
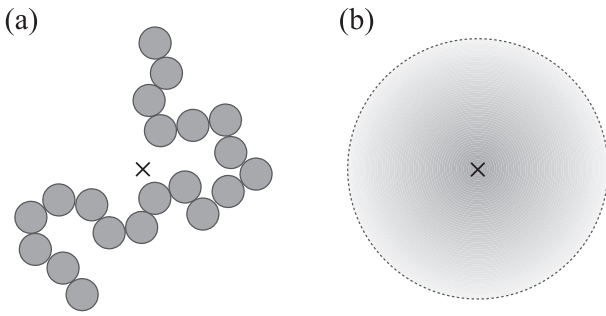
Figure 3. Schematic representation of (a) a MR polymer chain with $N = 20$ monomers, and (b) the CG representation of that chain. In both panels, the cross indicates the center of mass of the polymer.

forces in the CG model, f^{2b}, were parameterized using cubic splines with a uniform grid spacing Δr^{2b}. Thus, there are $K \equiv r_c^{2b}/\Delta r^{2b}$ grid points and basis functions which depend linearly on $2K$ spline coefficients λ_i. Imposing continuity and smoothness conditions, reduces the number of free coefficients to K. These coefficients were then determined by matching the forces in the CG representation to the ones from the MR simulations. To determine the K coefficients, we first divided the MR trajectory in blocks containing N_s snapshots each, and then solved the resulting set of $N_s N_p$ linear equations with a constrained least-squares algorithm for each block. Finally, we tabulated f^{2b} with a grid spacing of $\Delta r_{tab}^{2b} = 0.01\sigma$, averaging over the blockwise results. To ensure a smooth decay to zero at r_c^{2b}, we multiplied the tabulated forces with a smoothing function f^{sm} for all distances $r > r^{sm}$:

$$f^{sm}(r) = \cos\left(\frac{\pi}{2} \frac{r - r^{sm}}{r_c^{2b} - r^{sm}}\right).$$ (5)

The CG pair potential U^{2b} was then obtained by numerical integration of f^{2b}. This coarse-graining procedure is implemented in the VOTCA-CSG package [55].

The pair potential U_b^{2b} was determined from the MR melt simulations (see section 2.1) using a cutoff distance of $r_c^{2b} = 8\sigma$ and a grid spacing of $\Delta r^{2b} = 0.1\sigma$. Each block contained 300 frames, and the final potential was computed by taking the average of the 67 blocks. For computing U_0^{2b}, we

performed 64 independent simulations of two isolated polymers in a large simulation box ($L = 60\sigma$), so that they did not interact with their periodic images. The polymers were initialized at large distances and then approached each other due to the monomer–monomer attraction (see section 2.1). By evaluating the trajectories of these multiple runs, there were enough data for capturing the forces at all relevant distances. For the FM procedure for calculating U_0^{2b}, we used $r_c^{2b} = 8\sigma$ and $\Delta r^{2b} = 0.2\sigma$, averaging over 14 blocks each containing 750 000 frames. In both cases, we chose $r^{sm} = 7.5\sigma$.

2.2.2. Three-body interaction. Three-body interactions were taken into account using the Stillinger–Weber (SW) potential with flexible angular dependence, as implemented in the VOTCA-CSG package [29] and available under https://gitlab.mpcdf.mpg.de/votca

$$U^{SW}(r_{IJ}, r_{IK}, \theta_{IJK}) = f^{SW}(\theta_{IJK}) \exp\left(\frac{\eta}{r_{IJ} - r_c^{SW}}\right)$$
$$\times \exp\left(\frac{\eta}{r_{IK} - r_c^{SW}}\right),$$ (6)

with angle θ_{IJK} between the three particles (I being the central one), and angular interaction term $f^{SW}(\theta_{IJK})$. The cutoff distance r_c^{SW} determines how many triplets are included into the local environment of each CG polymer, and U^{SW} smoothly decays to zero when one of the two inter-particle distances r_{IJ} and r_{IK} reaches r_c^{SW}. The parameter η controls the steepness of this decay with small η corresponding to a steeper transition.

The angular dependence of U^{SW} allows for capturing anisotropic interactions, which occur near the polymer–solvent interfaces in the MR simulations (see figure 2). The angular interaction term $f^{SW}(\theta_{IJK})$ was fitted to the residual forces of the MR simulations $\Delta\mathbf{f}$ via the FM procedure [29]. We determined $\Delta\mathbf{f}$ acting on each CG polymer chain by subtracting the CG two-body force from the total reference force from the MR simulations, $\mathbf{f}_{MR}$:

$$\Delta\mathbf{f} = \mathbf{f}_{MR} - \mathbf{f}^{2b}.$$ (7)

In practice, we determined $\Delta\mathbf{f}$ by recomputing the forces acting on the centers of mass of the polymers in the MR

trajectories using the pairwise forces $\mathbf{f}^{2b}$. For $\mathbf{f}^{2b}$, we either used the forces due to U_b^{2b} or U_0^{2b} (see section 2.2.1). To distinguish the resulting three-body potentials, we will refer to them as $U_{\Delta b}^{SW}$ and $U_{\Delta 0}^{SW}$, respectively. The subscript 'Δ' indicates that the SW potential was parameterized using the residual forces $\Delta \mathbf{f}$ (equation (7)). Parameterization of U^{SW} according to $\Delta \mathbf{f}$ ensures the orthogonality of the two-body and three-body terms [29]. The fit parameters then depend on the choice of the pair potential, so that the additional three-body contribution can be regarded as a correction term to either U_b^{2b} or U_0^{2b}.

All trajectory reruns with pair potentials were carried out with the GROMACS simulation package [56]. All reruns with three-body potentials were carried out with the LAMMPS simulation package [57] with the user pair style sw/table [29] as available under https://gitlab.mpcdf.mpg.de/votca/lammps.

We used a cubic spline representation for $f^{SW}\left(\theta_{ijk}\right)$ with $K^{SW} = 31$ grid points and a linear dependence on the $2K^{SW}$ spline coefficients. Treating the two exponential terms in equation (6) as prefactors led to a linear set of equations which was solved by a constrained least-squares solver. For the thinnest films with $H \approx 4\,R_{g,b}$, we averaged over 200 blocks containing each 200 frames, while for the remaining systems we averaged over 800 blocks each containing 50 frames. We systematically varied the cutoff radius of $U_{\Delta b}^{SW}$ and $U_{\Delta 0}^{SW}$ from $r_c^{SW} = 4\,\sigma$ to $r_c^{SW} = 10\,\sigma$, and the parameter η from $\eta = \sigma$ to $\eta = 4\,\sigma$.

2.2.3. Local density-dependent interaction. Alternatively, many-body interactions were included in our CG simulations by supplementing the two-body pair potential with a local density-dependent potential (LDP). In this representation, each CG polymer carries a cloud, which effectively describes its monomers that were integrated out during the coarse-graining procedure (see figure 3). For simplicity, we assumed that the overlap of these clouds can be described by radial weight functions $\omega(r_{IJ})$, which only depend on the distance r_{IJ} between the CG particles I and J. In this work, we constructed the weight function $\omega(r_{IJ})$ by computing the pairwise overlap integral between the average monomer density clouds around the polymers centers of mass, $\rho_{cloud}(r)$. To determine $\omega(r_{IJ})$, we first computed $\rho_{cloud}(r)$ from the MR bulk simulations:

$$\rho_{cloud}(r) = \left\langle \frac{1}{N4\pi r^2} \sum_{i=1}^{N} \delta\left(|\mathbf{r}_i - \mathbf{r}_{com}| - r\right) \right\rangle, \quad (8)$$

where $\mathbf{r}_{com}$ is the center of mass position of the polymer. Assuming a pairwise overlap of the density clouds, the weight function $\omega(r_{IJ})$ is then given by:

$$\omega(r_{IJ}) = \int_V \rho_{cloud}(|\mathbf{r}_{com}^I - \mathbf{r}|)\rho_{cloud}(|\mathbf{r}_{com}^J - \mathbf{r}|)\, d^3\mathbf{r}. \quad (9)$$

Thus, $\omega(r_{IJ})$ can be interpreted as the number density of monomer pairs between a pair of (CG) polymers at center-to-center distance r_{IJ}. Figure 4 shows $\rho_{cloud}(r)$ as well as $\omega(r)$, which are both bounded and monotonically decrease with increasing r. The monomer density decays almost completely
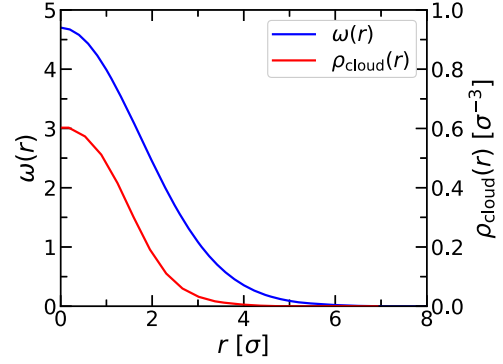
Figure 4. Weight function $\omega(r)$ (left axis) and monomer density around the polymer center of mass $\rho_{cloud}(r)$ (right axis) as functions of radial distance r.

at $r \approx R_{g,b}$ while $\omega(r)$ vanishes almost entirely at $r \approx 2\,R_{g,b}$, as expected.

The potential energy of CG particle I due to the LDP is then:

$$U_I^{LDP} = G(\varphi_I) \quad (10)$$

where G is an embedding function, and φ_I is the local density of (fictitious) monomer pairs at the position of CG particle I due to the other CG particles. We posit that φ_I can be expressed as the linear superposition of the pair density clouds of the other particles, that is:

$$\varphi_I = \sum_{J \neq I} \omega(r_{IJ}). \quad (11)$$

In this context, the embedding function G is a mean-field representation of many-body effects [58], and local density gradients enter the force calculation via the gradient of the embedding function. Thus, many-body effects are related to the curvature of G: if G is a linear function of φ_I, then the total potential reduces to a two-body pair potential. If G has a positive curvature, i.e., $d^2G/d\varphi^2 > 0$, then the LDP becomes more repulsive as the local density increases. Due to the assumed pairwise additivity of the weight functions $\omega(r_{IJ})$, the LDP can be interpreted as a generalized pair potential, which is why in practice LDPs are typically implemented as pair potentials [59–61]. Hence, the pressure tensor can be calculated as usual via the standard Clausius virial equation [62].

The embedding function was implemented as a cardinal B-spline function, with equally spaced nodes λ_i at distances $\Delta\varphi = 0.5$. This representation has the advantage that the derivatives with respect to the amplitude of the nodes, $\partial U^{LDP}/\partial\lambda_i$, are linear, which facilitates the calculation in the update step (see equation (15)). The number of nodes was adapted during the coarse-graining procedure to cover the required density range. We determined the embedding function G from our MR simulations using relative entropy minimization (REM) [20, 63]. The goal of this technique is to optimize the CG potential in such a way that the difference between the probability distribution of the MR configurations in the CG and the MR representation is minimized. This difference can be measured by the relative entropy, also known as the Kullback–Leibler divergence [64], which can be interpreted

as the difference in information conveyed by the probability distributions. So in contrast to other coarse-graining methods like FM or IBI, which are designed to reproduce the potential of mean force or the radial distribution function, respectively, REM aims to minimize the difference in the configurational probability distributions. As a consequence, the resulting CG potentials will differ, because there is in general no unique parameterization which optimizes *all* quantities of the target system.

In the canonical ensemble, the relative entropy can be written as:

$$S_{\text{rel}} = \beta \langle U_{\text{CG}} - U_{\text{MR}} \rangle_{\text{MR}} - \beta (A_{\text{CG}} - A_{\text{MR}}) + \langle S_{\text{map}} \rangle_{\text{MR}} \tag{12}$$

where U_{MR} and U_{CG} denote the potential functions, and A_{MR} and A_{CG} the configurational parts of the Helmholtz free energy for the MR and CG system, respectively. The term $\langle S_{\text{map}} \rangle_{\text{MR}}$ is the (unavoidable) contribution to the relative entropy due to the mapping. The relative entropy S_{rel} can be optimized using approximate and/or iterative methods to find a (locally) optimal set of parameters of the potential. In this work, we used a Newton–Raphson update rule to find the root of $\partial S_{\text{rel}}/\partial\lambda$, that is

$$\lambda^{j+1} = \lambda^j - \left(\frac{\partial S_{\text{rel}}}{\partial \lambda} \right) / \left(\frac{\partial^2 S_{\text{rel}}}{\partial \lambda^2} \right) \tag{13}$$

where j denotes the iteration. Here, the parameters to be optimized are the amplitudes of the nodes λ_i of the cardinal B-spline representation of the embedding function G. To improve the stability of the updates and the convergence of the optimization, we multiplied the change of the parameter $\Delta\lambda_i$ with a constant factor $\alpha = 0.01$ and clipped it at $\pm 1 k_B T$. The resulting update rule for the coefficients is then:

$$\lambda_i^{j+1} = \lambda_i^j - \Delta\lambda_i^j \tag{14}$$

$$\Delta\lambda_i^j = \min\left(-1, \max\left(1, \alpha\left[\left\langle \frac{\partial U^{\text{LDP}}}{\partial \lambda_i} \right\rangle_{\text{MR}} - \left\langle \frac{\partial U^{\text{LDP}}}{\partial \lambda_i} \right\rangle_{\text{CG}}\right]\right.\right.$$
$$\times \left[\left\langle \frac{\partial^2 U^{\text{LDP}}}{\partial (\lambda_i)^2} \right\rangle_{\text{MR}} - \left\langle \frac{\partial^2 U^{\text{LDP}}}{\partial (\lambda_i)^2} \right\rangle_{\text{CG}} + \beta\left\langle \left(\frac{\partial U^{\text{LDP}}}{\partial \lambda_i}\right)^2 \right\rangle_{\text{CG}}\right.$$
$$\left.\left.\left. - \beta\left\langle \frac{\partial U^{\text{LDP}}}{\partial \lambda_i} \right\rangle_{\text{CG}}^2\right]^{-1}\right)\right) \tag{15}$$

where $\langle\cdot\rangle_{\text{MR}}$ and $\langle\cdot\rangle_{\text{CG}}$ indicate averaging in the mapped MR and CG representation, respectively. For all investigated systems, we used 500 iterations with 200 000 simulation timesteps per iteration. All simulations with LDPs were carried out on graphics processing units with the HOOMD-blue simulation package (v. 2.4.2) [59–61].

3. Results

3.1. Two-body interactions

In a bulk polymer melt, every monomer is isotropically surrounded by other monomers, both from the same chain as from the other ones. Consequently, the intra- and inter-chain interactions compensate each other, and the polymers behave as
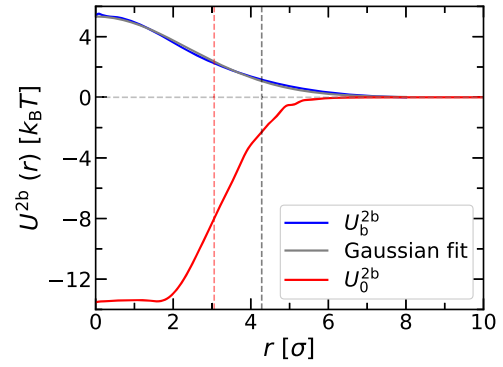

Figure 5. Pair potential acting between two CG polymers, computed from bulk melt simulations (U_b^{2b}, blue) and from simulations containing two isolated polymers (U_0^{2b}, red). The corresponding diameters of the polymers, $2 R_g$, from the MR simulations are indicated by a black and red vertical line, respectively.

dispersed in a Θ-solvent [2, 65, 66].[3] This does, however, *not* mean that the effective polymer–polymer interactions vanish, but that they are purely entropic instead. Figure 5 shows the effective pair potential between CG polymers in a melt, U_b^{2b}, which is repulsive and bounded, allowing a partial overlap of the CG polymers. This behavior is due to the fractal and open nature of the polymer coils, which lets the centers of mass of two coils be at the same place while each chain can fluctuate without intersecting the other (see figure 3(a)).

Previous consideration within renormalization-group theory [70] predicted that the effective potential can be approximated rather accurately by a Gaussian function $U_b^{2b} \propto \exp\left[-(r_{IJ}/\sigma_p)^2\right]$, with characteristic length-scale of the interaction σ_p. Our simulation data can be fitted perfectly to this functional form with $\sigma_p = 3.4\,\sigma$. Such Gaussian polymer–polymer interactions have also been reported in previous lattice [71] and off-lattice [1, 70] simulations of athermal polymer solutions. In particular, Louis *et al* varied the polymer concentration over a wide range, from dilute solutions up to almost five times the overlap concentration, finding that U_b^{2b} barely changed [1]. Further, they showed that U_b^{2b} reproduces rather accurately the equation of state of a polymer solution. However, a CG description of the polymers *only* in terms of U_b^{2b} is insufficient for modeling polymer films and droplets, as the CG polymers will repel each other rather than form a stable film, unless additional external constraints are applied.

The pair potential between two isolated polymers, U_0^{2b}, is attractive (see figure 5), resembling a soft square-well potential with a well depth of about $-13\,k_B T$ and a well width of roughly 2σ. This strong polymer–polymer attraction is due to the attractive tail of the LJ interaction between the monomers in the MR model (see equation (1)). At such low polymer concentrations, the employed MR model effectively describes polymers in a poor (implicit) solvent [52, 72, 73], which have collapsed into compact globules with a distinctly smaller radius of gyration compared to their coil-like analogs in the

---

[3] The Flory ideality theorem should be considered with care, however, as there are subtle differences in the static [67, 68] and dynamic [69] properties of ideal and real polymers..
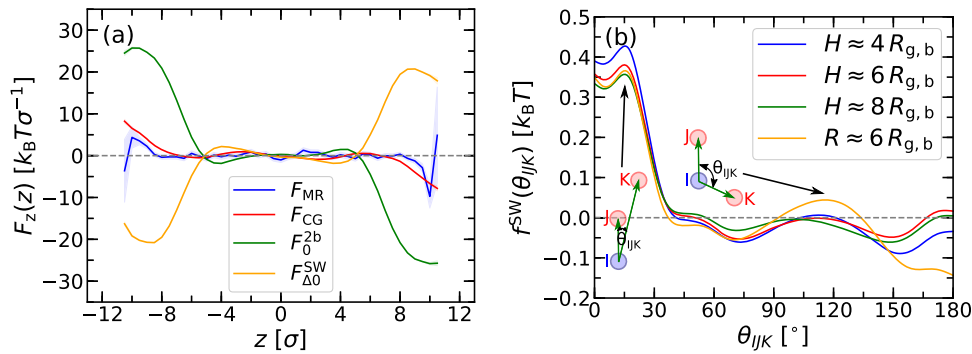
Figure 6. (a) Forces acting on the center of mass of the polymers perpendicular to the film surface, $F_z(z)$, as functions of z. Data shown for a film with thickness $H \approx 8\,R_{g,b}$. The blue curve corresponds to the net force in the MR simulation, while the red curve shows the net force using the CG potential. The green and orange curves show the two- and three-body contributions, U_0^{2b} and $U_{\Delta 0}^{SW}$, respectively. The shaded regions correspond to the measurement uncertainty determined from the standard error of the mean. (b) Angular part $f^{SW}(\theta_{IJK})$ of $U_{\Delta 0}^{SW}$ for films with different thicknesses H as indicated and droplet with radius $R \approx 6\,R_{g,b}$.

melt, i.e., $R_{g,0} \approx 1.5\,\sigma$ vs $R_{g,b} \approx 2.2\,\sigma$. Once two (or more) of these globules approach each other in the MR simulations, they coalesce into a small polymer droplet that remains stable over the investigated simulation time. However, simulations containing many CG polymers interacting only through U_0^{2b} behave in a nonphysical manner: due to the strong attraction for $r \lesssim 5\,\sigma$ and the lack of repulsive excluded volume interactions at short distances, the CG polymers merge into a single small aggregate, with a diameter that even *decreases* with increasing aggregation number. Alternatively, one could try to parameterize the pair potential at the Θ-temperature, where the solvent quality is exactly poor enough to cancel the polymer-swelling due to excluded volume effects, so that the polymer scales like an ideal chain. However, the resulting pair potential between two isolated polymers will be zero (apart from statistical fluctuations), leading to incorrect thermodynamic properties in the bulk and confined systems.

3.2. Three-body SW interactions

We determined the SW three-body potentials for the three different film systems, as well as for the droplet with radius $R \approx 6\,R_{g,b}$. For all investigated systems, the forces of the reference systems, $\mathbf{f}_{MR}$, were reproduced most faithfully when the residual forces $\Delta\mathbf{f}$ were fitted using U_0^{2b} with a cutoff distance of $r_c^{SW} = 10\,\sigma$. The dependence on η was weak and we chose $\eta = \sigma$ (see the supporting information (https://stacks.iop.org/JPCM/33/254002/mmedia) for a comparison of all different parameter combinations, as well as the results when fitting to the residual forces using U_b^{2b}).

Figure 6(a) shows the average force on the CG polymers perpendicular to the film surface, $F_z(z)$, in the film with $H \approx 8\,R_{g,b}$, where measurements were taken every $100\,\tau$. (The results for the other systems are qualitatively similar and are included in the supporting information.) In the MR simulations, the average net force on the center of mass of the polymers vanishes in the central bulk-like region of the film, $|z| < 6\,\sigma$ due to the film's symmetry along the z-axis. Further away from the film center, the net force on the polymers points inwards with its magnitude increasing the further the chain is located away from the film center. This net attraction

reflects the cohesive forces between the monomers in the MR simulations.

Using the particle positions from the MR trajectories (see section 2.2.2 for details), we computed the force profiles in the CG model and show the resulting profiles also in figure 6(a). The resulting net force has a similar shape as the reference force, although the flat plateau in the film center is replaced by a weak oscillation. The contribution from the two-body potential U_0^{2b} leads to a strong net attraction between the CG polymers, which is especially pronounced near the film surfaces because of the inhomogeneous polymer density distribution (see figure 2). The pairwise attraction in the CG model extends deep into the bulk region of the film, which is (partially) compensated by the repulsive three-body SW interactions. It should be noted, that these force profiles have been created using the CG model in trajectories from the MR reference simulations, and *not* from dedicated simulations using the CG model. Thus, the good agreement of the force profiles shown in figure 6(a) does not guarantee the stability of the films and droplets in the CG representation, which we will test in section 3.4.

In figure 6(b), we plot the angular part of the SW potential $f^{SW}(\theta_{IJK})$ for the three different films as well as for the droplet with radius $R \approx 6\,R_{g,b}$. The fitted functions $f^{SW}(\theta_{IJK})$ have similar shapes in all investigated cases, indicating a good transferability of the three-body potential. As the two exponential terms of the SW potential are strictly positive (see equation (6)), a positive (negative) sign of $f^{SW}(\theta)$ results in a net repulsion (attraction) between the central CG particle I of a triplet configuration and the two CG particles J and K. The SW potential is purely repulsive for small angles $\theta_{IJK} < 30°$, where the three CG polymers I, J, and K are lined up with J at a smaller distance and K at a larger distance behind chain J (see figure 6(c)). For larger angles $\theta_{IJK} > 30°$, $f^{SW}(\theta)$ oscillates around zero with a rather small amplitude.

3.3. Local density-dependent potentials

Using U_0^{2b} as the two-body potential between the CG polymers, we determined U_0^{LDP} for all films and droplets via
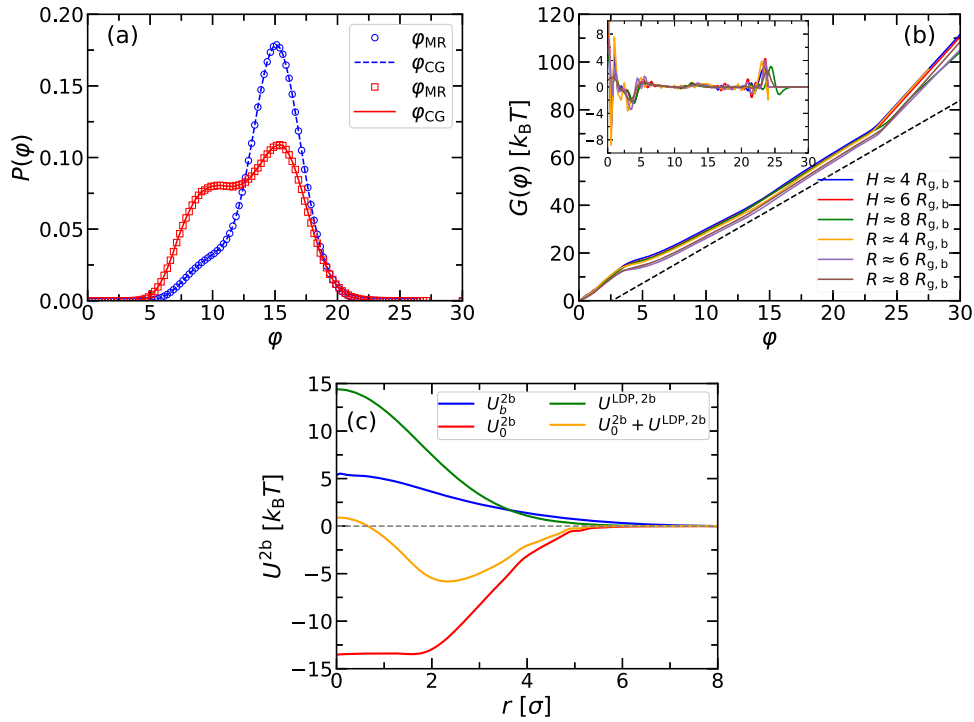
Figure 7. (a) Probability density function of the local density, $P(\varphi)$, in the MR (symbols) and CG systems (lines). Results for thin films ($H \approx 8\,R_{\mathrm{g,b}}$) are shown in blue, while results for droplets ($R \approx 4\,R_{\mathrm{g,b}}$) are shown in red. (b) Embedding functions, $G(\varphi)$, for all investigated systems. The dashed line indicates $G \propto \phi$, while the inset shows the second derivative $\mathrm{d}^2G/\mathrm{d}\varphi^2$. (c) Two-body interactions parameterized in the bulk simulations, $U_{\mathrm{b}}^{2\mathrm{b}}$, and effective two-body potential for the CG simulations with an LDP in the bulk region, $U_0^{2\mathrm{b}} + U^{\mathrm{LDP,2b}}$.

REM, as described in section 2.2.3. To verify that the coarse-graining procedure converged, we computed the probability density function of the local density, $P(\varphi)$, in both the mapped MR reference simulations as well as in the CG simulations. Figure 7(a) shows the corresponding results for the film with thickness $H \approx 8\,R_{\mathrm{g,b}}$ and the droplet with radius $R \approx 4\,R_{\mathrm{g,b}}$. The data for the CG and MR simulations are in perfect agreement, which indicates that the LDPs have been parameterized accurately. Small φ values correspond to polymers located near the polymer–solvent interface, while large φ values are associated with polymers in the central bulk-like region of the systems. All $P(\varphi)$ have a maximum near $\varphi \approx 15$, which indicates that there are more polymers in the bulk-like region than at the surfaces. This maximum becomes more pronounced as the film thickness H (droplet radius R) increases, because the surface-to-volume ratio decreases as $2/H$ ($3/R$). Note also, that a droplet with diameter $2R = H$ has a larger surface-to-volume ratio than a film with the same thickness, which is reflected by the larger $P(\varphi)$ values at small φ for droplets compared to films (see figure 7(a)).

Figure 7(b) shows the fitted embedding functions $G(\varphi)$ for all CG systems, which look nearly identical except for a slight vertical shift in the region $\varphi \gtrsim 4$. This good agreement indicates that the obtained LDPs are transferable across the different systems, that is, the embedding function $G(\varphi)$ parameterized for a small droplet is also applicable to a thick film. $G(\varphi)$ increases linearly with φ for $5 \leqslant \varphi \leqslant 22$, which corresponds to the range of local densities typically observed in the

films and droplets (see figure 7(a)). For such linear embedding functions $G(\varphi) = k\varphi + C$, the potential energy of particle I due to the LDP can be written as:

$$U_I^{\mathrm{LDP}} = C + k\varphi_I = C + \sum_{I \neq J} k\omega(r_{IJ}) = C + \sum_{I \neq J} U^{\mathrm{LDP,2b}}(r_{IJ}).$$

(16)

Hence, in this case, the LDP behaves like an additive pair potential $U^{\mathrm{LDP,2b}}(r)$, which restores the excluded volume interactions between the CG polymers. Figure 7(c) shows the resulting effective pair interaction between CG particles in the bulk-like region of the films and droplets, $U_0^{2\mathrm{b}} + U^{\mathrm{LDP,2b}}$, which is repulsive at short distances to prevent the CG particles from collapsing onto each other, and has a minimum at $r \approx R_{\mathrm{g,b}} = 2.2\,\sigma$ to achieve the desired inter-particle spacing in the bulk-like region. Outside the density region $5 \leqslant \varphi \leqslant 22$, the derivative $\mathrm{d}^2G/\mathrm{d}\varphi^2$ is nonzero (see inset of figure 7(b)), so that many-body effects become relevant. For smaller $\varphi < 5$, the derivative $\mathrm{d}^2G/\mathrm{d}\varphi^2$ is negative, so that U_0^{LDP} becomes less repulsive as the local density increases. In contrast, $\mathrm{d}^2G/\mathrm{d}\varphi^2 > 0$ for $\varphi > 22$, which ensures the incompressibility of the polymer film.

To assess the computational performance of the CG model, we performed bulk simulations with $N_{\mathrm{p}} = 2000$ polymers in a cubic box with edge length $L = 35.15\,\sigma$. Here, we found that the CG simulations using only the two-body interactions $U_{\mathrm{b}}^{2\mathrm{b}}$ achieved about 40 times more timesteps per second than the MR simulations, while the CG simulations with both $U_0^{2\mathrm{b}}$ and U_0^{LDP} achieved about 10 times more timesteps per second than the MR simulations. The actual speedup with respect to the
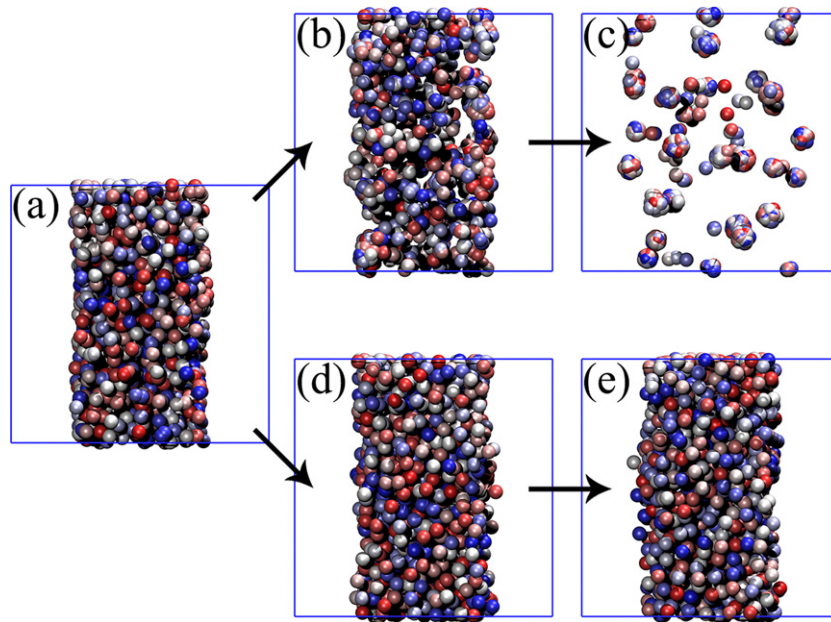
Figure 8. Snapshots of the CG simulations of the films with thickness $H \approx 8\,R_{\mathrm{g,b}}$. (a) Starting configuration. (b) and (c) CG simulations with U_0^{2b} and $U_{\Delta 0}^{SW}$ at $t = 2\,\tau$ and $4\,\tau$, respectively. (d) and (e) CG simulations with U_0^{2b} and U_0^{LDP} at $t = 2\tau$ and $40\,000\,\tau$, respectively.

physical timescales is likely even higher due to the accelerated dynamics in the soft CG models.

3.4. Stability of simulations

To investigate whether the CG representations using the SW potential or the LDP are able to reproduce stable films and droplets, we performed MD simulations using the CG models starting from the final snapshots of the MR reference simulations. Figure 8 shows typical snapshots of the CG simulations of the films with thickness $H \approx 8\,R_{\mathrm{g,b}}$ at different simulation times. The starting configuration is shown in figure 8(a), while the results from the runs with the SW potential and LDP are shown in figures 8(b), (c) and (d), (e), respectively.

The films in the CG simulations with U_0^{2b} and $U_{\Delta 0}^{SW}$ start to become unstable already after about $2\,\tau$, as the CG polymers collapse into small spherical aggregates, which are stabilized by a long range repulsion between them. The inability of this combination of two- and three-body interactions to reproduce the MR simulations even qualitatively stems likely from the restricted functional form of $U_{\Delta 0}^{SW}$. The residual force fit of the SW potential (see section 2.2.2) most probably only captures a local minimum of the potential of mean force, whereas the global minimum of the fitted CG model corresponds to this collapsed state. This transition can be better understood by considering the strong attraction of U_0^{2b} at short distances (see figure 5), whereas the three-body contribution $U_{\Delta 0}^{SW}$ is repulsive only for small angles $\theta_{IJK} < 30°$, where three CG beads are lined up as shown in figure 6(b). Thus, small deviations in θ_{IJK} are already sufficient to overcome the repulsive barrier between neighboring particles. This interpretation is corroborated by the distribution of angles θ_{IJK} in the collapsed droplets, where we find almost no triplets with angles in the range of $\theta_{IJK} < 30°$. CG simulations with U_b^{2b} and $U_{\Delta b}^{SW}$ do not reproduce stable films or droplets either, as in these cases

the (attractive) three-body contribution $U_{\Delta b}^{SW}$ is not sufficient to compensate the repulsive pair potential U_b^{2b} (see the supporting information for the fitting results of $U_{\Delta b}^{SW}$). In addition, including SW interactions with a relatively large cutoff ($r_c^{SW} = 10\sigma$) significantly slows down the CG simulations due to the large number of triplets included into the force calculation. In fact, the CG simulations became less efficient than the original MR ones.

In contrast, the CG simulations with the pair potential U_0^{2b} and LDP U_0^{LDP} lead to stable film and droplet configurations, even after long simulation times (see figure 8). (Note that simulations using the effective pair interactions U_0^{2b} and $U^{LDP,2b}$, see section 3.3, exhibit a similar instability as the simulations with U_0^{2b} and $U_{\Delta 0}^{SW}$.) To investigate the resulting configurations in more detail, we computed the density profiles along the z-axis for the films and in the radial direction for the droplets. The corresponding results for the film with thickness $H \approx 8\,R_{\mathrm{g,b}}$ and the droplet with radius $R \approx 4\,R_{\mathrm{g,b}}$ are plotted in figure 9. Again the measurement uncertainties of the density profiles are estimated from the standard error of the mean between ten subdivided blocks of the data. Overall, the density profiles in the CG simulations are reasonably close to the ones from the MR simulations, with relative deviations of H and R below 4%, and similar polymer densities in the central region of the films and droplets. However, the polymer–solvent interfaces are slightly broader in the CG simulations, which is also reflected by the smaller surface tension measured in the CG simulations, that is $\gamma = 0.31 \pm 0.01\,k_\mathrm{B}T/\sigma^2$ vs $\gamma = 1.42\,k_\mathrm{B}T/\sigma^2$ for the planar films. Further, the peaks in the density profiles near the polymer–solvent interfaces are slightly more pronounced and more narrow in the MR simulations compared to the CG simulations. This difference can be understood if one considers the oblate ellipsoidal shape of the polymers at the interfaces in the MR simulations (see figure 2(b)). This shape anisotropy
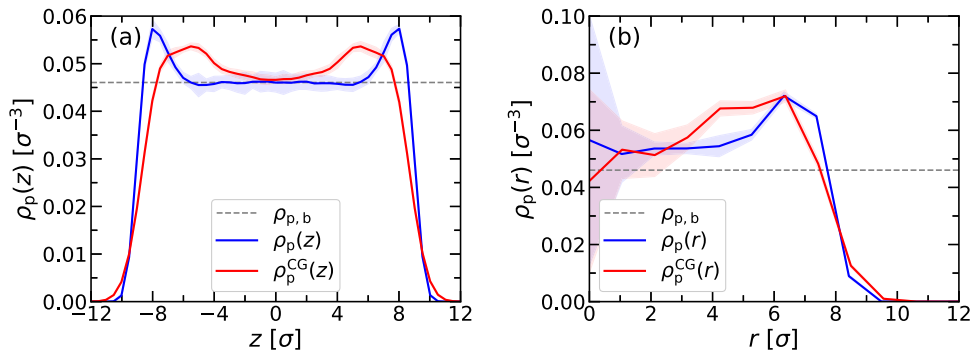
Figure 9. Number density profiles of polymer centers of mass of the mapped MR reference (ρ_p) and CG simulations (ρ_p^{CG}) for (a) a film with thickness $H \approx 8\,R_{g,b}$, and (b) a droplet with radius $R \approx 4\,R_{g,b}$. The horizontal dashed line indicates the polymer number density in the bulk system. In both panels, the shaded regions correspond to the measurement uncertainty determined from the standard error of the mean.
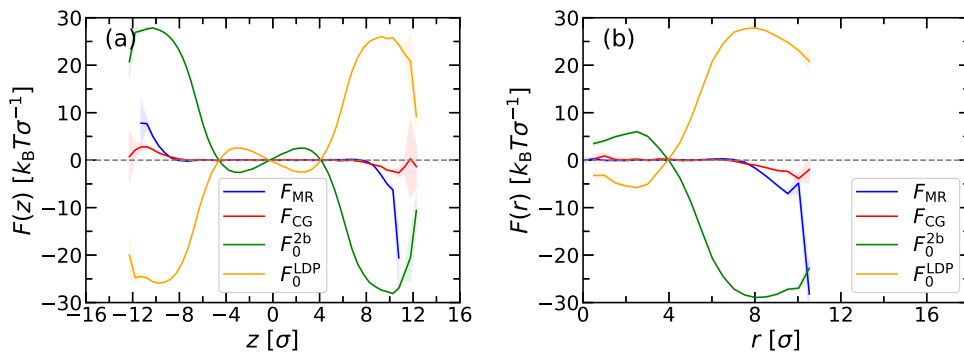
Figure 10. Force profiles for (a) a film with thickness $H \approx 8\,R_{g,b}$ and (b) a droplet with radius $R \approx 4\,R_{g,b}$ as functions of z or r, respectively. The blue curve corresponds to the net force in the MR simulation, while the red curve shows the net force in the CG simulations. The green and orange curves show the two-body and LDP contributions, U_0^{2b} and U_0^{LDP}, respectively. In both panels, the shaded regions correspond to the measurement uncertainty determined from the standard error of the mean.

near the polymer–solvent interface can, however, not be captured by our CG model, where the polymers are modeled as soft spheres.

In addition, we computed the force profiles along the z-axis in the films and in the radial direction r for the droplets (see figure 10). The force profiles were calculated as the mean forces of particles at the given z or r position with data taken every $100\,\tau$. In both the MR and CG simulations, the net force is essentially zero in the central region of the film and droplet, due to the symmetry of the systems. Polymers near the surface of the film/droplet experience attractive forces toward the center of the film/droplet. These cohesive forces are stronger and act on a much narrower region in the MR simulations compared to the CG simulations. If one decomposes the net force into the contributions from the two- and many-body interactions, one sees that U_0^{2b} and U_0^{LDP} have opposite signs and are each significantly larger than the resulting net force. Both forces also extend much further into the central region of the films and droplets than expected from the width of the bumps at the extremities of the force profiles. Evidently, the stability of the films and droplets is the result of a delicate balance between two- and many-body interactions in our CG model.

4. Conclusions

We developed CG models of homopolymers, where each polymer was represented by a single (soft) spherical particle and the solvent was included implicitly. We focused on simulations of thin films and droplets with strong density inhomogeneities near the polymer–solvent interfaces. In CG simulations where the polymers interacted only through two-body potentials, the films and droplets either dissolved or collapsed into small aggregates, depending on whether the effective polymer–polymer interactions were parameterized in reference simulations in the bulk or at infinite dilution. These CG representations failed at capturing (even qualitatively) the main physical characteristics of the reference systems, because they did not correctly reproduce the cohesive forces and the compressibility of the polymers, respectively.

To address these inherent issues, we supplemented the two-body potentials by additional three-body or many-body interactions, which were parameterized in the inhomogeneous systems. The three-body interactions were represented by a Stillinger–Weber potential which was fitted to the residual forces of the MR reference simulations. Many-body interactions were included in a mean-field way via local density-

dependent interactions, which were optimized using the REM technique. The CG models with three-body interactions failed at maintaining stable polymer films or droplets, and the CG particles collapsed into small spherical aggregates instead. In contrast, the CG simulations with local density-dependent interactions reproduced stable films and droplets with linear dimensions close to the reference simulations, except that the polymer–solvent interfaces were slightly sharper and the accompanied surface tension was higher in the reference simulations. We attributed these differences to the deformation of polymers near the interfaces, which could not be resolved in the CG representation, where the polymers were mapped to spherical beads. In future work, we plan to enhance our model to capture such effects. Further, we want to develop analytic expressions for the pair- and many-body interactions to avoid (or at least minimize) running microscopically resolved reference simulations for parameterizing the CG model.

Acknowledgments

Data availability statement

The data that support the findings of this study are available upon reasonable request from the authors.

ORCID iDs

Fabian Berressem ⃝ https://orcid.org/0000-0002-7658-938X
Christoph Scherer ⃝ https://orcid.org/0000-0003-2587-4567
Denis Andrienko ⃝ https://orcid.org/0000-0002-1541-1377
Arash Nikoubashman ⃝ https://orcid.org/0000-0003-0563-825X

References

[1] Louis A A, Bolhuis P G, Hansen J P and Meijer E J 2000 Can polymer coils Be modeled as 'soft colloids'? *Phys. Rev. Lett.* **85** 2522
[2] Likos C N 2001 Effective interactions in soft condensed matter physics *Phys. Rep.* **348** 267–439
[3] Zhang G, Chazirakis A, Harmandaris V A, Stuehn T, Daoulas K C and Kremer K 2019 Hierarchical modelling of polystyrene melts: from soft blobs to atomistic resolution *Soft Matter* **15** 289–302
[4] Zacharopoulos N, Vergadou N and Theodorou D N 2005 Coarse graining using pretabulated potentials: liquid benzene *J. Chem. Phys.* **122** 244111

[5] Mullinax J W and Noid W G 2010 A generalized-Yvon–Born–Green theory for determining coarse-grained interaction potentials *J. Phys. Chem.* C **114** 5661–74
[6] Mullinax J W and Noid W G 2010 Reference state for the generalized Yvon–Born–Green theory: application for coarse-grained model of hydrophobic hydration *J. Chem. Phys.* **133** 124107
[7] Murtola T, Bunker A, Vattulainen I, Deserno M and Karttunen M 2009 Multiscale modeling of emergent materials: biological and soft matter *Phys. Chem. Chem. Phys.* **11** 1869–92
[8] Marrink S J, Risselada H J, Yefimov S, Tieleman D P and de Vries A H 2007 The MARTINI force field: coarse grained model for biomolecular simulations *J. Phys. Chem.* B **111** 7812–24
[9] Huang D M, Faller R, Do K and Moulé A J 2010 Coarse-grained computer simulations of polymer/fullerene bulk heterojunctions for organic photovoltaic applications *J. Chem. Theory Comput.* **6** 526–37
[10] Lukyanov A, Malafeev A, Ivanov V, Chen H-L, Kremer K and Andrienko D 2010 Solvated poly-(phenylene vinylene) derivatives: conformational structure and aggregation behavior *J. Mater. Chem.* **20** 10475–85
[11] Rühle V, Kirkpatrick J, Kremer K and Andrienko D 2008 Coarse-grained modelling of polypyrrole morphologies *Phys. Status Solidi b* **245** 844–8
[12] Gemünden P, Poelking C, Kremer K, Andrienko D and Daoulas K C 2013 Nematic ordering, conjugation, and density of states of soluble polymeric semiconductors *Macromolecules* **46** 5762–74
[13] Scherer C and Andrienko D 2016 Comparison of systematic coarse-graining strategies for soluble conjugated polymers *Eur. Phys. J.: Spec. Top.* **225** 1441–61
[14] Greco C, Melnyk A, Kremer K, Andrienko D and Daoulas K C 2019 Generic model for lamellar self-assembly in conjugated polymers: linking mesoscopic morphology and charge transport in P3HT *Macromolecules* **52** 968–81
[15] Villa A, Peter C and van der Vegt N F A 2009 Self-assembling dipeptides: conformational sampling in solvent-free coarse-grained simulation *Phys. Chem. Chem. Phys.* **11** 2077–86
[16] Shinoda W, DeVane R and Klein M L 2008 Coarse-grained molecular modeling of non-ionic surfactant self-assembly *Soft Matter* **4** 2454–62
[17] Monticelli L, Kandasamy S K, Periole X, Larson R G, Tieleman D P and Marrink S-J 2008 The MARTINI coarse-grained force field: extension to proteins *J. Chem. Theory Comput.* **4** 819–34
[18] Noid W G, Chu J-W, Ayton G S, Krishna V, Izvekov S, Voth G A, Das A and Andersen H C 2008 The multiscale coarse-graining method. I. A rigorous bridge between atomistic and coarse-grained models *J. Chem. Phys.* **128** 244114
[19] Rudzinski J F and Noid W G 2011 Coarse-graining entropy, forces, and structures *J. Chem. Phys.* **135** 214101
[20] Shell M S 2008 The relative entropy is fundamental to multiscale and inverse thermodynamic problems *J. Chem. Phys.* **129** 144108
[21] Chaimovich A and Shell M S 2011 Coarse-graining errors and numerical optimization using a relative entropy framework *J. Chem. Phys.* **134** 094112
[22] Mashayak S Y, Jochum M N, Koschke K, Aluru N R, Rühle V and Junghans C 2015 Relative entropy and optimization-driven coarse-graining methods in VOTCA *PLoS One* **10** 1–20
[23] Kalligiannaki E, Chazirakis A, Tsourtis A, Katsoulakis M A, Plecháč P and Harmandaris V 2016 Parametrizing coarse grained models for molecular systems at equilibrium *Eur. Phys. J.: Spec. Top.* **225** 1347–72
[24] Izvekov S and Voth G A 2005 Multiscale coarse graining of liquid-state systems *J. Chem. Phys.* **123** 134105

[25] Noid W G, Liu P, Wang Y, Chu J-W, Ayton G S, Izvekov S, Andersen H C and Voth G A 2008 The multiscale coarse-graining method. II. Numerical implementation for coarse-grained molecular models *J. Chem. Phys.* **128** 244115

[26] Lyubartsev A P and Laaksonen A 1995 Calculation of effective interaction potentials from radial distribution functions: a reverse Monte Carlo approach *Phys. Rev.* E **52** 3730

[27] Tóth G 2007 Effective potentials from complex simulations: a potential-matching algorithm and remarks on coarse-grained potentials *J. Phys.: Condens. Matter* **19** 335222

[28] Henderson R L 1974 A uniqueness theorem for fluid pair correlation functions *Phys. Lett.* A **49** 197–8

[29] Scherer C and Andrienko D 2018 Understanding three-body contributions to coarse-grained force fields *Phys. Chem. Chem. Phys.* **20** 22387–94

[30] Louis A A 2002 Beware of density dependent pair potentials *J. Phys.: Condens. Matter* **14** 9187–206

[31] Peter C and Kremer K 2009 Multiscale simulation of soft matter systems - from the atomistic to the coarse-grained level and back *Soft Matter* **5** 4357–66

[32] Bereau T, Bennett W F D, Pfaendtner J, Deserno M and Karttunen M 2015 Folding and insertion thermodynamics of the transmembrane WALP peptide *J. Chem. Phys.* **143** 243127

[33] Kanduč M and Netz R R 2017 Atomistic simulations of wetting properties and water films on hydrophilic surfaces *J. Chem. Phys.* **146** 164705

[34] Binder K 1981 Critical properties from Monte Carlo coarse graining and renormalization *Phys. Rev. Lett.* **47** 693

[35] Svaneborg C, Karimi-Varzaneh H A, Hojdis N, Fleck F and Everaers R 2016 Multiscale approach to equilibrating model polymer melts *Phys. Rev.* E **94** 032502

[36] Jin J and Voth G A 2018 Ultra-coarse-grained models allow for an accurate and transferable treatment of interfacial systems *J. Chem. Theory Comput.* **14** 2180–97

[37] Jochum M, Andrienko D, Kremer K and Peter C 2012 Structure-based coarse-graining in liquid slabs *J. Chem. Phys.* **137** 064102

[38] Mashayak S Y and Aluru N R 2012 Coarse-grained potential model for structural prediction of confined water *J. Chem. Theory Comput.* **8** 1828–40 PMID: 26593674

[39] Montes-Saralegui M, Kahl G and Nikoubashman A 2017 On the applicability of density dependent effective interactions in cluster-forming systems *J. Chem. Phys.* **146** 054904

[40] Das A and Andersen H C 2012 The multiscale coarse-graining method. IX. A general method for construction of three body coarse-grained force fields *J. Chem. Phys.* **136** 194114

[41] Bereau T, Andrienko D and von Lilienfeld O A 2015 Transferable atomic multipole machine learning models for small organic molecules *J. Chem. Theory Comput.* **11** 3225–33

[42] Shapeev A V 2016 Moment tensor potentials: a class of systematically improvable interatomic potentials *Multiscale Model. Simul.* **14** 1153–73

[43] Nguyen T T, Székely E, Imbalzano G, Behler J, Csányi G, Ceriotti M, Götz A W and Paesani F 2018 Comparison of permutationally invariant polynomials, neural networks, and Gaussian approximation potentials in representing many-body expansions *J. Chem. Phys.* **148** 241725

[44] Glielmo A, Zeni C and De Vita A 2018 Efficient nonparametric *n*-body force fields from machine learning *Phys. Rev.* B **97** 184307

[45] Scherer C, Scheid R, Andrienko D and Bereau T 2020 Kernel-based machine learning for efficient simulations of molecular liquids *J. Chem. Theory Comput.* **16** 3194–204

[46] Allen E C and Rutledge G C 2008 A novel algorithm for creating coarse-grained, density dependent implicit solvent models *J. Chem. Phys.* **128** 154115

[47] Faure G, Maillet J-B and Stoltz G 2014 Local density dependent potential for compressible mesoparticles *J. Chem. Phys.* **140** 114105

[48] DeLyser M R and Noid W G 2017 Extending pressure-matching to inhomogeneous systems via local-density potentials *J. Chem. Phys.* **147** 134111

[49] DeLyser M R and Noid W G 2019 Analysis of local density potentials *J. Chem. Phys.* **151** 224106

[50] Bishop M, Kalos M H and Frisch H L 1979 Molecular dynamics of polymeric systems *J. Chem. Phys.* **70** 1299–304

[51] Kremer K and Grest G S 1990 Dynamics of entangled linear polymer melts: a molecular-dynamics simulation *J. Chem. Phys.* **92** 5057–86

[52] Midya J, Egorov S A, Binder K and Nikoubashman A 2019 Phase behavior of flexible and semiflexible polymers in solvents of varying quality *J. Chem. Phys.* **151** 034902

[53] Humphrey W, Dalke A and Schulten K 1996 VMD: Visual molecular dynamics *J. Mol. Graphics* **14** 33–8

[54] Binder K, Müller M, Schmid F and Werner A 2001 'Intrinsic' profiles and capillary waves at interfaces between coexisting phases in polymer blends *Adv. Colloid Interface Sci.* **94** 237–48

[55] Rühle V, Junghans C, Lukyanov A, Kremer K and Andrienko D 2009 Versatile object-oriented toolkit for coarse-graining applications *J. Chem. Theory Comput.* **5** 3211–23

[56] Abraham M J, Murtola T, Schulz R, Páll S, Smith J C, Hess B and Lindahl E 2015 GROMACS: high performance molecular simulations through multi-level parallelism from laptops to supercomputers *SoftwareX* **1-2** 19–25

[57] Plimton S 1995 Fast parallel algorithms for short-range molecular dynamics *J. Comput. Phys.* **117** 1–19

[58] Berendsen H J C, Grigera J R and Straatsma T P 1987 The missing term in effective pair potentials *J. Phys. Chem.* **91** 6269–71

[59] Anderson J A, Glaser J and Glotzer S C 2020 HOOMD-blue: a Python package for high-performance molecular dynamics and hard particle Monte Carlo simulations *Comput. Mater. Sci.* **173** 109363

[60] Morozv I V, Kazennova A M, Bystryia R G, Normana G E, Pisareva V V and Stegailova V V 2011 Molecular dynamics simulations of the relaxation processes in the condensed matter on GPUs *Comput. Phys. Commun.* **182** 1974–8

[61] Yang L, Zhang F, Wang C-Z, Ho K-M and Travesset A 2018 Implementation of metal-friendly EAM/FS-type semi-empirical potentials in HOOMD-blue: a GPU-accelerated molecular dynamics software *J. Comput. Phys.* **359** 352–60

[62] Frenkel D and Smit B 2001 *Understanding Molecular Simulation: From Algorithms to Applications* (New York: Academic)

[63] Sanyal T and Shell M S 2016 Coarse-grained models using local-density potentials optimized with the relative entropy: application to implicit solvation *J. Chem. Phys.* **145** 034109

[64] Kullback S and Leibler R A 1951 On information and sufficiency *Ann. Math. Statist.* **22** 79–86

[65] Flory P J 1988 *Statistical Mechanics of Chain Molecules* (New York: Oxford University Press)

[66] Rubinstein M and Colby R H 2003 *Polymer Physics* (Oxford: Oxford University Press)

[67] Wittmer J P, Beckrich P, Johner A, Semenov A N, Obukhov S P, Meyer H and Baschnagel J 2007 Why polymer chains in a melt are not random walks *Europhys. Lett.* **77** 56003

[68] Meyer H, Horwath E and Virnau P 2018 Mapping onto ideal chains overestimates self-entanglements in polymer melts *ACS Macro Lett.* **7** 757–61

[69] Meyer H, Wittmer J P, Kreer T, Beckrich P, Johner A, Farago J and Baschnagel J 2008 Static Rouse modes and related quantities: corrections to chain ideality in polymer melts *Eur. Phys. J.* E **26** 25–33

[70] Krüger B, Schäfer L and Baumgärtner A 1989 Correlations among interpenetrating polymer coils : the probing of a fractal *J. Phys.* **50** 3191–222

[71] Olaj O F and Pelinka K H 1976 Pair distribution function and pair potential of lattice model chains under theta conditions, 1. Numerical evaluation *Makromol. Chem.* **177** 3413–25

[72] Reddy G and Yethiraj A 2006 Implicit and explicit solvent models for the simulation of dilute polymer solutions *Macromolecules* **39** 8536–42

[73] Huissmann S, Blaak R and Likos C N 2009 Star polymers in solvents of varying quality *Macromolecules* **42** 2806–16